

Pion-nucleus elastic scattering on ^{12}C , ^{40}Ca , ^{90}Zr , and ^{208}Pb at 400 and 500 MeV

George Kahrmanis,^{1,α} George Burleson,² C. M. Chen,⁴, B. C. Clark⁴, Kalvir Dhuga,⁵
D. J. Ernst,⁶ J. A. Faucett,^{2,β} H. T. Fortune,⁷ S. Hama,⁸ Ahmed Hussein,⁹ M. F. Jiang,⁶
K. W. Johnson,¹ L. Kurth Kerr⁴, Scott Mathews,⁵ John McGill,^{10,γ} C. Fred Moore,¹ Shaul
Mordechai,¹¹ Christopher L. Morris,¹⁰ John O'Donnell,^{7,β} Mike Snell,¹ Mohini
Rawool-Sullivan,¹⁰ L. Ray,¹ Charles Whitley,^{1,β} and Allen L. Williams^{1,δ}

¹ *Department of Physics, University of Texas at Austin, Austin, Texas 78712-1081*

² *Department of Physics, New Mexico State University, Las Cruces, New Mexico 88003*

³ *Saint John's and Saint Mary's Institute of Technology, #499 Sec. IV Tam-King Rd., Tam-Sui,
Taiwan 23135*

⁴ *Department of Physics, The Ohio State University, Columbus, Ohio 43210*

⁵ *Department of Physics, George Washington University, Washington, DC 20052*

⁶ *Department of Physics and Astronomy, Vanderbilt University, Nashville, Tennessee 37235*

⁷ *Department of Physics and Astronomy, University of Pennsylvania, Philadelphia, Pennsylvania
19104*

⁸ *Hiroshima University of Economics, Hiroshima 731-01, Japan*

⁹ *University of Northern British Columbia, Prince George, British Columbia, Canada V2N 4Z9*

¹⁰ *Los Alamos National Laboratory, Los Alamos, New Mexico, 87545*

¹¹ *Ben-Gurion University of the Negev, Beer-Sheva 84105, Israel*

α Current address: 2808 35th Street #5E, Long Island City, New York 11103

β Currently at Los Alamos National Laboratory

γ Currently at the University of Texas at Austin

*δ Currently at the Johns Hopkins Oncology Center, Division of Radiation Oncology, 600 North
Wolf Street, Baltimore, Maryland 21287-8922*

Abstract

Pion-nucleus elastic scattering at energies above the $\Delta(1232)$ resonance is studied using both π^+ and π^- beams on ^{12}C , ^{40}Ca , ^{90}Zr , and ^{208}Pb . The present data provide an opportunity to study the interaction of pions with nuclei at energies where second-order corrections to impulse approximation calculations should be small. The results are compared with other data sets at similar energies, and with four different first-order impulse approximation calculations. Significant disagreement exists between the calculations and the data from this experiment.

25.80.Dj, 24.10.-i

I. INTRODUCTION

The study of π^\pm -nucleus elastic differential scattering cross sections with incident pion energy above 300 MeV, *i.e.*, beyond the range of the first pion-nucleon resonance, $\Delta(1232)$, has been motivated by several considerations. Because the wavelength of the pion is shorter at higher energies it can be a sensitive probe of spatial distributions in a nucleus. The pion-nucleon two-body interaction becomes weaker above resonance allowing the pion to penetrate deeper into the nucleus. The two-body total cross section drops to 25 mb (isospin-averaged) at 500 MeV, about 18% of its value on the peak of the resonance. In addition, the smaller two-body cross section implies that second-order corrections to first-order multiple-scattering optical potentials should be small. Thus, significant differences between the measured elastic cross sections and the first-order impulse approximation (IA) calculations, especially at forward angles, could signal the failure of the IA which would pose a number of interesting physics questions.

At energies above the Δ , pion elastic differential cross sections at 800 MeV/c were measured at BNL for ^{12}C and ^{40}Ca [1]. The data were in qualitative agreement with a number of different calculations, however the differential cross sections at forward angles were underpredicted by all of them [2–7]. The 15% normalization error in the data, as well as some uncertainties in the input to the calculations, caused difficulty in pin-pointing the reasons for the discrepancy. More recent pion-nucleus data at 400 MeV for ^{28}Si from LAMPF [8] and for ^{12}C at 610, 710, 790, and 895 MeV/c and ^{208}Pb at 790 MeV/c from KEK [9–11] are now available. The overall agreement between theory and experiment is qualitative at best for ^{12}C but is quite reasonable for ^{208}Pb . As will be discussed below, the discrepancy at forward angles is less pronounced for these data than for the BNL data or the present experiment.

In Sec. II the experiment is described. Section III briefly discusses the four theoretical calculations which are compared with the present experimental data. Comparisons with previous data are also given. A summary is given in Sec. IV.

II. EXPERIMENT

In this work we present elastic scattering data for π^\pm on ^{12}C , ^{40}Ca , ^{90}Zr , and ^{208}Pb at pion laboratory kinetic energies of 400 and 500 MeV. The data were taken at the Los Alamos Meson Physics Facility. At 400 MeV one is still on the high-energy tail of the Δ . At 500 MeV, the pion-nucleon center-of-mass total energy is 1451 MeV which is near the P_{11} (1440), the next resonance above the $\Delta(1232)$.

Data were obtained using the P^3 east channel at the Clinton P. Anderson Meson Physics Facility and the Large Acceptance Spectrometer (LAS). The P^3 channel provides a pion beam, produced by interactions of the 800 MeV primary proton beam in the ^{12}C production target. In the original design the pion beam was achromatic at the experimental target, *i.e.*, the mean momentum of the incident pions would not be correlated with position. For the purposes of this work a dispersed beam tune was developed in order to improve the resolution in the missing mass spectra. With this tune the momentum dispersion at the target was $0.5\%/cm$. The angle of incidence was also correlated with position at the target. The energy spread of the incident pion beam was about 10 MeV at the 400 MeV setting and about 12 MeV at the 500 MeV setting.

The outgoing pions were detected using a modified version of the Argonne Large Acceptance Spectrometer, a Q-Q-D system. Four drift chamber planes, measuring both horizontal and vertical positions and angles, were located between the second quadrupole magnet and the dipole magnet. Four wire chamber planes followed by two sets of scintillators were located after the analyzing dipole magnet. All of the wire chambers were delay-line-readout drift chambers [12]. In order to minimize Coulomb multiple scattering and improve the momentum resolution helium bags were installed along the entire six-meter distance from the target to the rear wire chambers, the target was enclosed in a vacuum chamber, and thin ($6\ \mu\text{m}$ mylar) windows were used on the wire chambers. The apparatus included an additional sweep magnet between the target and the spectrometer which was adjusted to bend the paths of particles with the nominal momentum of the spectrometer setting by 10° in the

horizontal plane, and to steer particles of the opposite charge away from the spectrometer. The acceptance of the spectrometer was $\pm 5^\circ$ in scattering angle (horizontally), $\pm 2.5^\circ$ in the vertical direction, and $\pm 10\%$ in $\Delta p/p$.

Three beam monitors were used, each supplying a relative measurement of the integrated current for every run. A toroidal counter, located just downstream of the production target, monitored the proton beam. An ion chamber was located in the production target box. Another ion chamber was placed at the exit of the beam pipe. With any fixed beam tune the ratio of any two beam-monitor readouts was constant within 1%. The hardware trigger consisted of a coincidence between any front-chamber signals with the two scintillators at the end of the spectrometer. The target thicknesses were 290 mg/cm^2 for CH_2 , 541 mg/cm^2 for ^{12}C , 400 mg/cm^2 for ^{40}Ca , 672 mg/cm^2 for ^{90}Zr and 421 mg/cm^2 for ^{208}Pb . The nominal target thickness error is 3% for each target. The ^{90}Zr and ^{208}Pb targets were enriched in isotopic purity to greater than 95% and the C and Ca targets were of natural isotopic abundance.

The scattered pion momentum, the coordinates and angles at the target location were calculated using Taylor series expansions about the central trajectory through the spectrometer. In addition, redundancy checks (we measured four positions and four angles to describe trajectories given by two positions, two angles and one momentum) were calculated as differences between the measured rear angles and rear angles calculated using all coordinate information excluding the rear angle measurements. The polynomial coefficients for the target positions were calibrated by using horizontal and vertical rod targets. Coefficients for the angle calculations were obtained by using the beam at reduced intensity and changing the angle by moving the spectrometer around zero degrees. The coefficients for the momentum calculation were obtained by scanning an elastic peak across the focal plane of the spectrometer.

The beam momentum–position correlation at the target was directly measured using data taken with a heavy target, ^{208}Pb , for which finite angular resolution effects on the missing mass spectra are small since the recoil energies are insignificant compared to the

scattered pion kinetic energy. The resulting width for the elastic peak in the missing mass spectra of the heavier targets was as small as 1.7 MeV for beam energies of 400 MeV.

The calculation of missing mass include the recoil energy with scattering angle, measured in the spectrometer. The effect of a correlation in the beam direction with target position on the scattering angle was included in this calculation. These effects are important for scattering from hydrogen because of the large variation in kinetic energy with scattering angle of more than 1 MeV/deg at large angles. The finite angular resolution, due to both angular dispersion in the beam and the resolution of the angle determination in the spectrometer, limited the missing mass resolution for hydrogen. By comparing the width of the ^{208}Pb elastic peak with the corresponding elastic peak for hydrogen at the same scattering angle we obtained a direct measure of our angular resolution, which was 1.2° FWHM.

The measurement of position and angles both before and after the spectrometer dipole provided a useful capability for rejecting particles that underwent collisions or decay downstream from the target. The rear angles were calculated as a polynomial of front positions, front angles, and momentum. The difference between the calculated and measured angle was typically about 2 mrad. Good events were selected with a cut on this quantity of ± 5 mrad.

A combination of pulse-height and time-of-flight information from the scintillators was used to reject proton events. Figure 1 shows the separation of proton events from those of lighter particles, in a two-dimensional histogram of the time of flight *vs.* the geometric mean of the heights of the pulses coming from the two scintillators. This technique was not able to distinguish pions from electrons and muons. Electrons were eliminated by using a Cherenkov counter in the focal plane and muons due to pion decays in the spectrometer were eliminated by the angle checks. The fraction of events due to muons elastically scattered in the target is estimated to be smaller than 0.001 [13].

Figure 2 shows typical missing-mass spectra at $T_\pi = 400$ MeV and $\theta_{lab} = 33^\circ$ (averaged over 8°). Typically there are several peaks in each missing-mass histogram, corresponding to the ground state and several excited states of the target nucleus. We fitted each histogram

with a Gaussian peak shape. The overlap between the ground-state peak and the inelastic peaks was usually small, since the resolution was 1.7 MeV FWHM at $T_\pi = 400$ MeV, and about 1.9 MeV FWHM at 500 MeV.

Each set of data was partitioned into 0.5° bins in the angle of scattering (in lab coordinates). In each experimental run (*i.e.* for each spectrometer setting, target, incoming energy, and pion polarity) we recorded data that spanned 17 bins. We incremented the angle of the spectrometer settings by 6° , so that any two adjacent settings had five bins in common.

The uncertainty in the absolute scattering angle was estimated to be ± 0.85 deg which arises from the uncertainty in the absolute zero degree scattering position (± 0.60 deg) and the locations of the survey marks on the floor (± 0.25 deg) for the spectrometer angle settings. The absolute scattering angles were determined (to ± 0.60 deg) by placing the spectrometer in the beam and by measuring the energy difference between the elastic peaks for pion scattering from ^1H and ^{208}Pb and using kinematics to determine the scattering angle.

The normalization involved two stages. First, we found each bin's relative normalization (referred to as the relative component of acceptance) with respect to all other bins for the same beam tune and target dimensions (the height of the ^{90}Zr target was smaller than the rest of the targets, so we used a separate normalization for those runs). This relative normalization was fixed for given target dimensions and beam tune, regardless of the spectrometer angle. Then, for each beam tune and target shape we determined an overall normalization such that $\pi - p$ scattering data from CH_2 matched the Arndt partial-wave fit to the corresponding pion-nucleon cross section [14].

The relative component of the acceptance of each run was treated as a function of two variables, the momentum of the particle (more precisely, the fractional deviation from the nominal setting of the spectrometer) and the bin number. With fixed beam tune and target dimensions, this function was fixed, independent of target material or spectrometer angle. The dependence of the relative component of acceptance of each bin on momentum was found by varying the momentum setting of the spectrometer and comparing yields.

The dependence on the bin number was found by comparing yields at the same angle in several overlapping runs. The latter method was complemented by a trial adjustment of the 17 relative bin acceptances so that the resulting cross sections smoothly matched as well as possible in χ^2 to a high order polynomial (order 15 to 19 worked best). The fitting involved data from several targets and resulted in no significant modification of the previous acceptance coefficients. The relative normalization procedure proved quite robust when the statistics were adequate.

The overall normalization uncertainty in this experiment is 16%. This error arises from several components: 3% in the target thickness (which is counted twice, since it applies to the normalization targets as well), 4% in each overall normalization coefficient, 1% in the beam count, 1% in the isotopic purity, 1% in each bin's relative normalization coefficient, an estimated 10% arising from the systematic error we describe next, and an uncertainty of 11%, at most, in determining the efficiency of the detection setup.

The only significant systematic error in this experiment arises from treating the relative component of the acceptance of each bin as a function of two variables only, while there was indication of a small dependence upon at least another variable; that might be, for instance, a target coordinate. But our statistical sample was inadequate for taking that effect into account. Instead, we have estimated its contribution to the overall uncertainty.

III. DISCUSSION AND ANALYSIS

The present experimental elastic differential cross sections are compared with four different theoretical first-order IA calculations. All have been used previously to investigate pion and kaon nucleus elastic scattering. The first model discussed is based on the relativistic impulse approximation (RIA) which has been used with success in describing proton-nucleus scattering [15,16]. For the scattering of spin zero mesons the Kemmer-Duffin-Petiau (KDP) equation [17–19] rather than the Dirac equation is used. This KDP-RIA approach has been used to obtain optical potentials for both kaon-nucleus and pion-nucleus elastic scatter-

ing [2,20–22]. The construction of the Lorentz scalar and vector optical potentials parallels that of the usual RIA. The two-body input consists of scalar and vector neutron and proton mean-field Hartree densities [23] and the empirical meson-nucleon Arndt amplitudes [14].

These calculations are shown by solid lines in Figs. 3 through 6. As in the Dirac case, the scalar and vector potentials are large and tend to cancel. These optical potentials, along with the Coulomb potential obtained from the empirical charge distribution from electron scattering, are used in the second-order KDP wave equation which is solved by partial wave analysis to get the elastic scattering differential cross sections. A non-relativistic impulse approximation, NRIA, optical potential is also obtained using the same Arndt amplitudes and the same vector neutron and proton mean-field Hartree densities, see Ref. [20]. These results are given by the dotted lines in Figs. 3 through 6. These optical potentials, along with the Coulomb potential, are used in the Schrödinger equation and the observables are obtained by partial wave analysis. Both calculations include the effect of folding over the 1.20° FWHM angular resolution uncertainty.

As mentioned above, although the scalar and vector potentials are very large, in some cases over 1500 MeV at the origin, the resulting effective central potentials are modest in size. In Fig. 7 we show the KDP-RIA real and imaginary potentials for $\text{Pb}(\pi^\pm, \pi^\pm)$ at 400, 500 and 662.6 MeV. The NRIA potentials are also shown for 500 MeV. The imaginary central potentials are remarkably energy independent. This is true for all of the targets considered in this work. The values of the volume integral per nucleon, J/A , are between -240 and -280 MeV-fm³ for all targets and energies. The real central potentials exhibit more energy dependence but they are always repulsive in this energy range [24].

It is of interest to compare the two models above with results from the more complete momentum-space multiple-scattering optical potential, ROMPIN, developed by Chen, Ernst, and Johnson [3–5]. These authors have obtained a first-order optical potential which uses covariant kinematics, phase-space factors and normalizations, off-shell two-body amplitudes, and exact Fermi-averaging integrals. The momentum-space optical potential is used in a Klein-Gordon equation and the differential cross sections are obtained. The results of the

ROMPIN calculations are shown by dashed lines in Figs. 3 through 5. In addition, the authors of Ref. [3] have developed an eikonal model for comparison with their “model-exact” calculation. The eikonal calculations are given by the dot-dashed curves in Figs. 3 through 6. Both the momentum-space optical and eikonal models use the same on-shell pion amplitudes [14] and the same Hartree-Fock wave functions [25,26] which have been corrected for center-of-mass motion. Both calculations have been folded over the 1.2° FWHM angular resolution uncertainty.

The first observation is that all of these four calculations agree with each other to within 10%-15% at small angles. The noticeable differences at larger angles could reasonably be attributed to differences in the nuclear structure input, the differences in the construction of the optical potentials, and the different one-body equations used. Other explanations are, of course, possible. The calculations generally agree better with each other than they do with the data. This is especially true as the target mass increases. The difference between the measured small angle differential cross sections and the calculated values is pronounced for all targets at both energies, though it is difficult to see this clearly on the log-scale of the figures [24]. In addition, there is a systematic difference between theory and experiment regarding the position of the first diffraction minima. In every case the first minima for both the KDP-RIA and the ROMPIN calculations occur at angles which are 1.0° to 2.0° larger than the corresponding minima in the data. In a similar analysis of the 400 MeV $^{28}\text{Si}(\pi^\pm, \pi^\pm)$ LAMPF data, the position of the diffraction dip is in much better agreement with experiment than evidenced here for any of the targets [20]. Both of these features will be discussed again when comparisons with other experimental data are given.

In Fig. 8 the KEK, BNL, and LAMPF $^{12}\text{C}(\pi^-, \pi^-)$ differential cross sections are plotted as a function of the momentum transfer q . Because all four of the calculations described above agree with each other at forward angles, *i.e.* up to the first diffraction minima, only the KDP-RIA calculations are shown. The calculations agree with the forward angle cross sections to within the normalization errors except for the 800 MeV/c BNL data and the 400 and 500 MeV LAMPF data. In every case, except for the 710 MeV/c KEK data, the

diffraction minima in the KDP-RIA calculations occur at angles about 1.5° to 2.0° larger than the minima in the data. In these calculations recoil is not taken into account, however the ROMPIN calculations do address the question of recoil and, as is shown in Fig. 3, the ROMPIN and KDP-RIA dip positions agree to within 0.5° , so the reason for the discrepancy is not clear. The results for $^{12}\text{C}(\pi^+, \pi^+)$ at 400 and 500 MeV and 800 MeV/c shown in Fig. 9 also indicate a similar result regarding the position of the diffraction minima. The calculated small angle cross sections for 800 MeV/c underpredict the BNL data but overpredict the LAMPF data.

Figures 10 and 11 compare the $^{40}\text{Ca}(\pi^\pm, \pi^\pm)$ BNL results with those of the present experiment. The underprediction of the small angle BNL data is evident. However, the positions of the diffraction minima are well reproduced by the calculations, in disagreement with the results for the current experiment where the minima are shifted. Of course, it is possible to fit the 400 and 500 MeV data by a simple two-parameter scaling of the potentials, but this does not give much insight into the origin of the discrepancy. Figures 12 and 13 show the results for $^{208}\text{Pb}(\pi^\pm, \pi^\pm)$. The higher energy data at 790 MeV/c (662.7 MeV) are from KEK [9,11]. The disagreement between the present experiment and the calculations is profound while agreement with the KEK data is reasonable. The 10% uncertainty in the elementary amplitudes does not result in calculated cross sections which resolve the discrepancy [24]. Using more recent determinations of the relativistic mean-field Hartree densities, which incorporate nonlinear chiral symmetry and broken scale invariance [27], do not change the results [24]. Referring to the central potentials shown in Fig. 7 does not reveal any anomalous behaviour with energy. It is possible that some of this discrepancy may be accounted for by the absolute angle uncertainty (0.85°) in the data, but not all of it. At this time a full understanding of the source of the diffraction minima angle discrepancy is not available.

IV. SUMMARY

Pion-nucleus elastic scattering at energies above the $\Delta(1232)$ resonance has been studied using both π^+ and π^- beams on ^{12}C , ^{40}Ca , ^{90}Zr , and ^{208}Pb targets. These new data were compared with other data sets at similar energies and with four theoretical calculations. Certain aspects of the predictions are in qualitative agreement with the data; however significant disagreements are seen, particularly in the angular positions of the diffractive minima, which are generally not evidenced in comparisons with other experiments. This is particularly true for ^{90}Zr and ^{208}Pb . The cause of these discrepancies has not yet been identified, and may wait until other experiments using heavy targets become available in this energy range.

ACKNOWLEDGMENTS

This work was supported in part by the United States Department of Energy, the Robert A. Welch Foundation, the U.S.–Israel Binational Science Foundation, and the National Science Foundation.

REFERENCES

- [1] D. Marlow, P.D. Barnes, N.J. Colella, S.A. Dytman, R.A. Eisenstein, R. Grace, P. Pile, F. Takeuchi, W.R. Wharton, S. Bart, D. Hancock, R. Hackenberg, E. Hungerford, W. Mayes, L. Pinsky, T. Williams, R. Chrien, H. Palevsky, R. Sutter, *Phys. Rev. C* **30**, 1662 (1984).
- [2] B.C. Clark, S. Hama, G.R. Kälbermann, R.L. Mercer, L. Ray, *Phys. Rev. Lett.* **55**, 592 (1985).
- [3] C.M. Chen, D.J. Ernst, Mikkel B. Johnson, *Phys. Rev. C* **48**, 841 (1993).
- [4] C.M. Chen, D.J. Ernst, and M.B. Johnson, *Phys. Rev. C* **47**, R9 (1993).
- [5] M.B. Johnson and D.J. Ernst, *Ann. Phys.* **219**, 266 (1992).
- [6] Masaki Arima, Keiichi Masutani, Ryoichi Seki, *Phys. Rev. C* **44**, 415 (1991).
- [7] Masaki Arima, Keiichi Masutani, Ryoichi Seki, *Phys. Rev. C* **51**, 431 (1995).
- [8] M.W. Rawool-Sullivan, C.L. Morris, J.M. O'Donnell, R.M. Whitten, B.K. Park, G.R. Burleson, D.L. Watson, J. Johnson, A.L. Williams, D.A. Smith, D.J. Ernst, C.M. Chen, *Phys. Rev. C* **49**, 627 (1994).
- [9] T. Takahashi, Ph.D. dissertation, Kyoto University (1995).
- [10] T. Takahashi, H. Sakaguchi, K. Aoki, T. Hasegawa, O. Hashimoto, T. Nagae, M. Sekimoto, A. Ohkusu, H. Bhang, H. Yu, and Y. Gavrilov, *Phys. Rev. C* **51**, 2542 (1995).
- [11] T. Takahashi, Proceedings of the 23rd INS Symposium, Tokyo, Japan, March 1995.
- [12] L. G. Atencio, J. F. Amann, R. L. Boudrie, and C. L. Morris, *Nucl. Instrum. and Meth.* **187**, 381 (1981).
- [13] Richard Werbeck and Robert Macek, "Performance of the High-Energy Pion Beam at LAMPF", *IEEE Transactions on Nuclear Science*, Vol.NS-22, No.3, June 1975.

- [14] R. A. Arndt, J. S. Hyslop and L. D. Roper, Phys. Rev. D **35**, 127 (1987); Richard A. Arndt, Igor I. Strakovsky, Ron L. Workman, Marcello M. Pavan, Phys. Rev. C **52**, 2120 (1995); R.A. Arndt, SAID program, private communication.
- [15] B. C. Clark, S. Hama, R. L. Mercer, L. Ray and B. D. Serot, Phys. Rev. Lett. **50**, 1644 (1983).
- [16] L. Ray, G.W. Hoffmann and W.R. Coker, Phys. Rep. **212**, 223 (1992).
- [17] N. Kemmer, Proc. Roy. Soc. London, Ser. **A173**, 91 (1939).
- [18] R.J. Duffin, Phys. Rev. **54**, 1114 (1938).
- [19] G. Petiau, Acad. Roy. Belg. Cl. Sci. Mom. Collect. 6 **16**, No. 2 (1936).
- [20] L.J. Kurth, B.C. Clark, E.D. Cooper, S. Hama, R.L. Mercer, L. Ray, G.W. Hoffmann, Phys. Rev. C **50**, 2624 (1994).
- [21] R. Michael, M.B. Barakat, S. Bart, R.E. Chrien, B.C. Clark, D.J. Ernst, S. Hama, K.H. Hicks, E.V. Hungerford, M.F. Jiang, T. Kishimoto, C.M. Kormanyos, L.J. Kurth, L. Lee, B. Mayes, R.J. Peterson, L. Pinsky, R. Sawafta, R. Sutter, L. Tang, J.E. Wise, Phys. Lett. B **382**, 29 (1996).
- [22] L.J. Kurth, B.C. Clark, E.D. Cooper, S. Hama, R.L. Mercer, L. Ray, G.W. Hoffmann, Nucl. Phys. **A585**, 335c (1995).
- [23] R.J. Furnstahl, C.E. Price and G.W. Walker, Phys. Rev. C **36**, 2590 (1987); Case C densities.
- [24] Figures showing the KDP-RIA scalar, vector, and effective central potentials, tabulations of the calculated and experimental small angle cross sections, and figures showing the effects of changing the input amplitudes and densities in the KDP-RIA calculations are available for all targets and energies from bcc@mps.ohio-state.edu or kurth@mps.ohio-state.edu.

- [25] J.W. Negele, Phys. Rev. C **1**, 1260 (1969).
- [26] M. Beiner, H. Flocard, N. Van Gai, and P. Quentin, Nucl. Phys. **A238**, 29 (1975).
- [27] R.J. Furnstahl, Hua-Bin Tang, Brian D. Serot, Phys. Rev. C **52**, 1368 (1995); Case T1 densities.

FIGURES

FIG. 1. 2-d histogram of time of flight *vs* the geometric mean of the pulse heights from the two scintillators, $S2$ and $S3$. Events in the upper group are identified as protons, and those inside the selected box as pions or lighter particles. The latter are few, and are expected to be almost totally rejected by further kinematic tests. The data were taken with ^{208}Pb , the central scattering angle set at 12° , and $T_\pi = 500$ MeV. The scales are linear and are in arbitrary units.

FIG. 2. Un-normlized missing-mass spectra of π^- scattering at incoming energy 400 MeV, central scattering angle set at 33° , from ^{12}C , ^{40}Ca , ^{90}Zr , and ^{208}Pb . The bin size is 100 keV. The number of events has not been folded with acceptance, which varies with the missing mass. In the cases of ^{90}Zr and ^{208}Pb , there are excited states between the 2^+ and 3^- states.

FIG. 3. The differential cross sections for $^{12}\text{C}(\pi^\pm, \pi^\pm)$ at 400 MeV (scaled by 10^{-1}) and 500 MeV (scaled by 10^{+1}). The solid curves are from KDP-RIA calculations, the dashed curves are from ROMPIN calculations, the dotdash curves are from eikonal calculations, and the dotted curves are from NRIA calculations.

FIG. 4. The differential cross sections for $^{40}\text{Ca}(\pi^\pm, \pi^\pm)$ at 400 MeV (scaled by 10^{-1}) and 500 MeV (scaled by 10^{+1}). The solid curves are from KDP-RIA calculations, the dashed curves are from ROMPIN calculations, the dotdash curves are from eikonal calculations, and the dotted curves are from NRIA calculations.

FIG. 5. The differential cross sections for $^{90}\text{Zr}(\pi^+, \pi^+)$ at 400 and 500 MeV and $^{90}\text{Zr}(\pi^-, \pi^-)$ at 400 MeV. The solid curves are from KDP-RIA calculations, the dashed curves are from ROMPIN calculations, the dotdash curves are from eikonal calculations, and the dotted curves are from NRIA calculations.

FIG. 6. The differential cross sections for $^{208}\text{Pb}(\pi^\pm, \pi^\pm)$ at 400 MeV (scaled by 10^{-1}) and 500 MeV (scaled by 10^{+1}). The solid curves are from KDP-RIA calculations, the dotdash curves are from eikonal calculations, and the dotted curves are from NRIA calculations. ROMPIN calculations were not available for this target.

FIG. 7. The real and imaginary effective central potentials for $^{208}\text{Pb}(\pi^+, \pi^+)$ and $^{208}\text{Pb}(\pi^-, \pi^-)$. Solid curves are for KDP-RIA at 400 MeV, dashed are KDP-RIA at 500 MeV, dotdash are NRIA at 500 MeV and dotted are KDP-RIA at 662.6 MeV (790 MeV/c).

FIG. 8. The KEK, BNL, and LAMPF $^{12}\text{C}(\pi^-, \pi^-)$ differential cross sections as a function of the momentum transfer q . Solid curves are from KDP-RIA calculations. (A) shows LAMPF data at 400 MeV scaled by 10^{+7} , (B) shows KEK data at 486.2 MeV (610 MeV/c) scaled by 10^{+5} , (C) shows LAMPF data at 500 MeV scaled by 10^{+3} , (D) shows KEK data at 584.02 MeV (710 MeV/c) scaled by 10^{+1} , (E) shows KEK data at 662.7 MeV (790 MeV/c) scaled by 10^{-1} , (F) shows BNL data at 672.5 MeV (800 MeV/c) scaled by 10^{-3} , and (G) shows KEK data at 766.2 MeV (895 MeV/c) scaled by 10^{-5} .

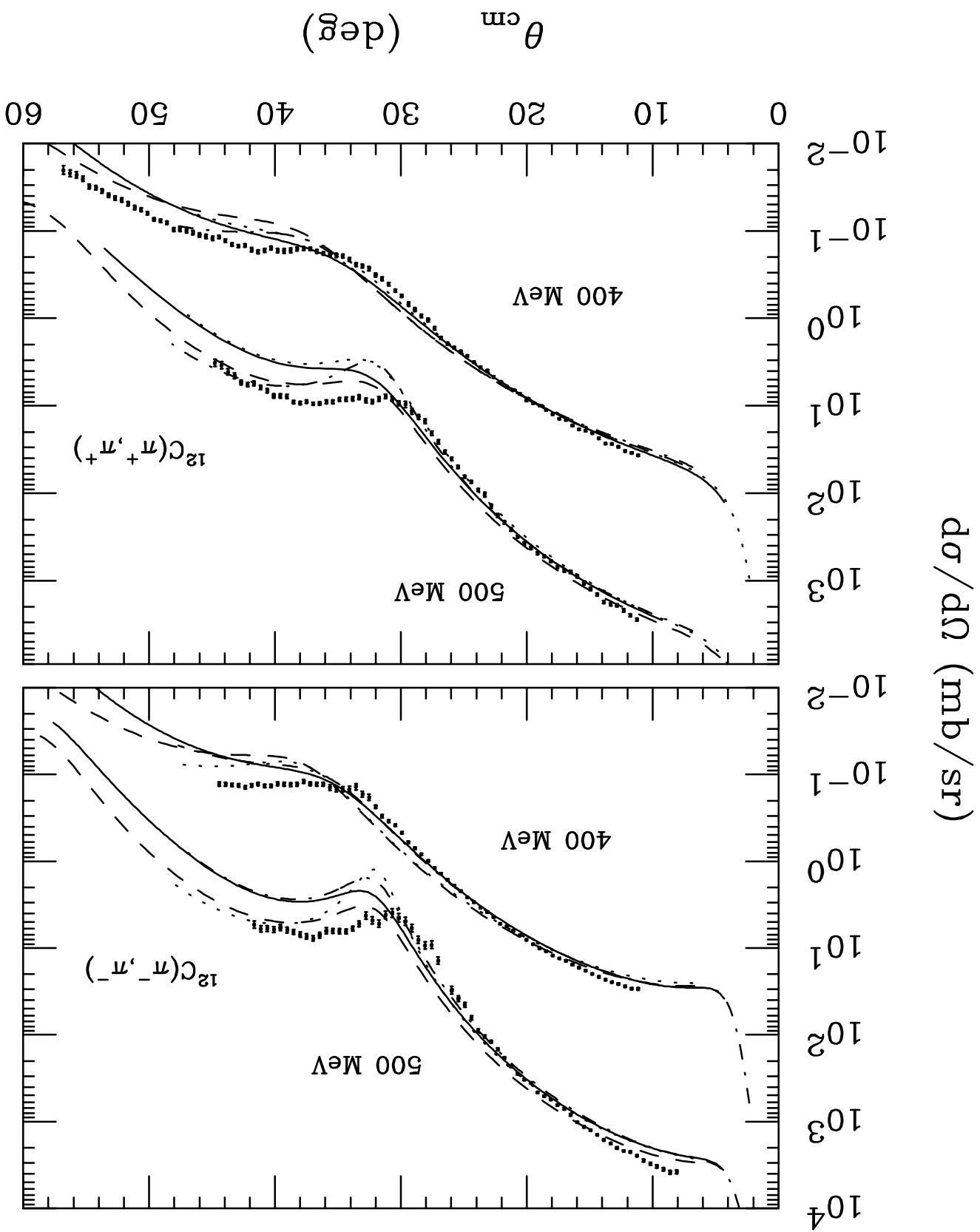
FIG. 9. $^{12}\text{C}(\pi^+, \pi^+)$ differential cross sections at 400, 500, and 672.5 MeV. The 400 and 500 MeV data are from this experiment and 672.5 MeV (800 MeV/c) data are from BNL. Curves are from KDP-RIA calculations.

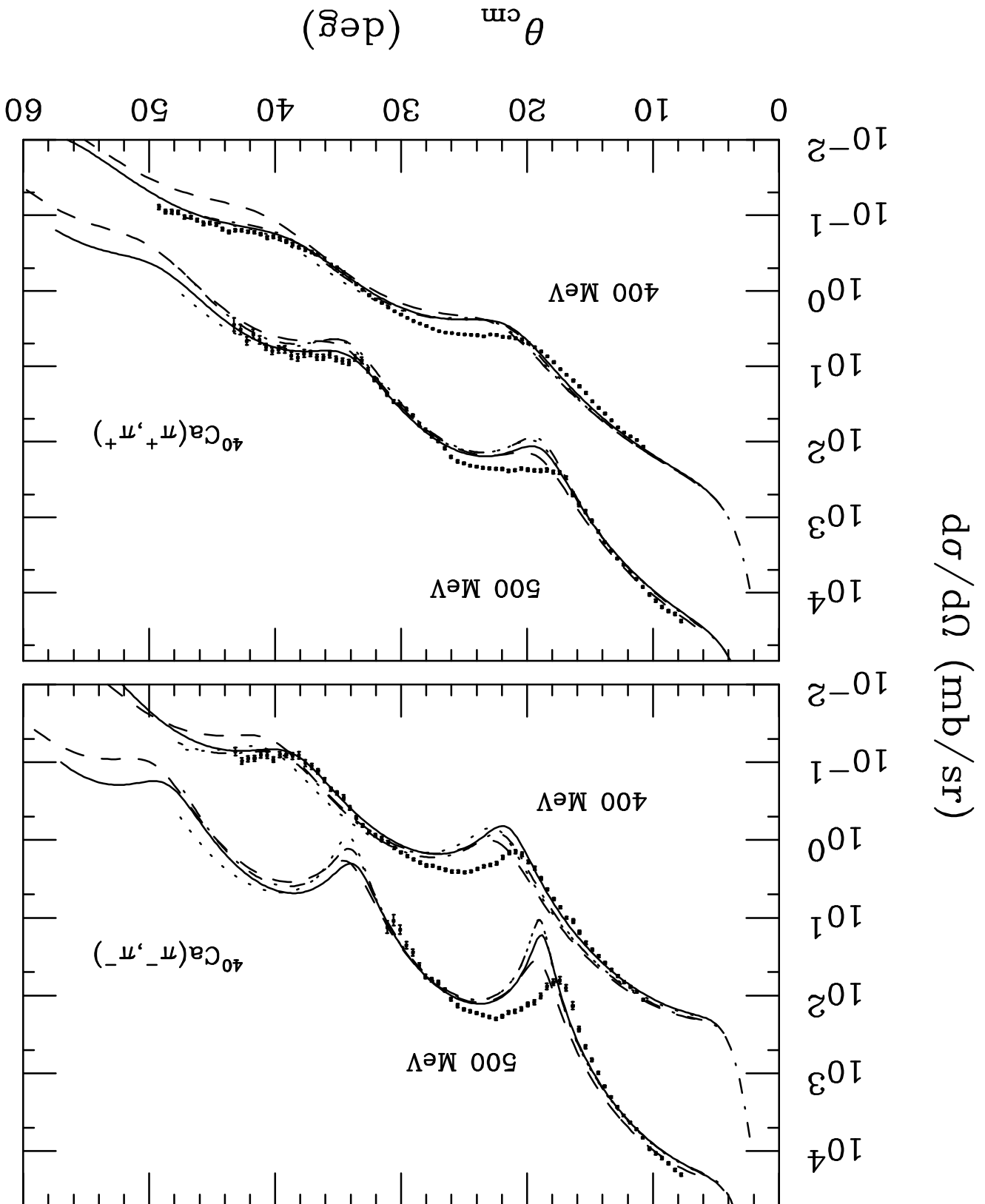
FIG. 10. $^{40}\text{Ca}(\pi^+, \pi^+)$ differential cross sections at 400, 500, and 672.5 MeV. The 400 and 500 MeV data are from this experiment and 672.5 MeV (800 MeV/c) data are from BNL. Curves are from KDP-RIA calculations.

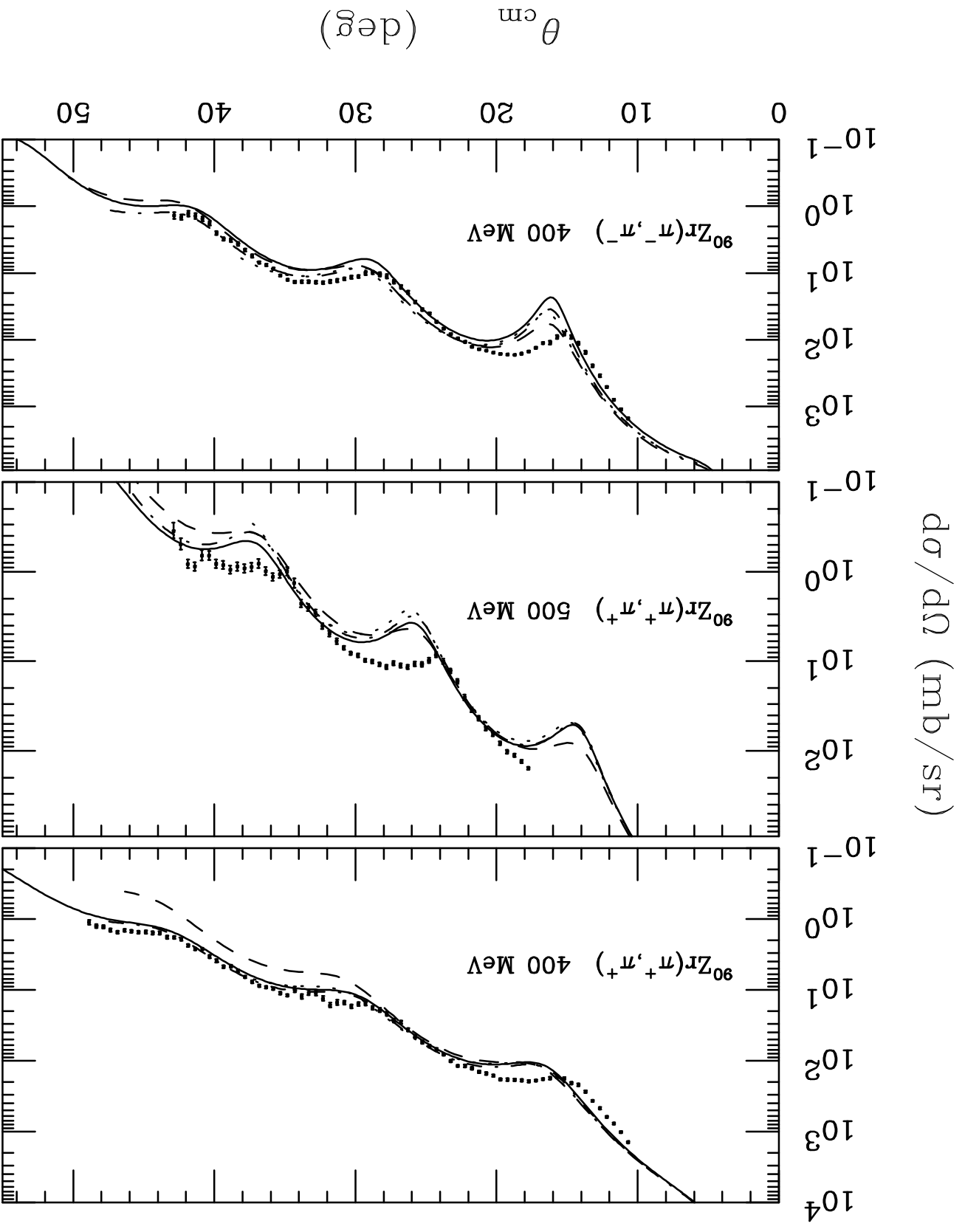
FIG. 11. $^{40}\text{Ca}(\pi^-, \pi^-)$ differential cross sections at 400, 500, and 672.5 MeV. The 400 and 500 MeV data are from this experiment and 672.5 MeV (800 MeV/c) data are from BNL. Curves are from KDP-RIA calculations.

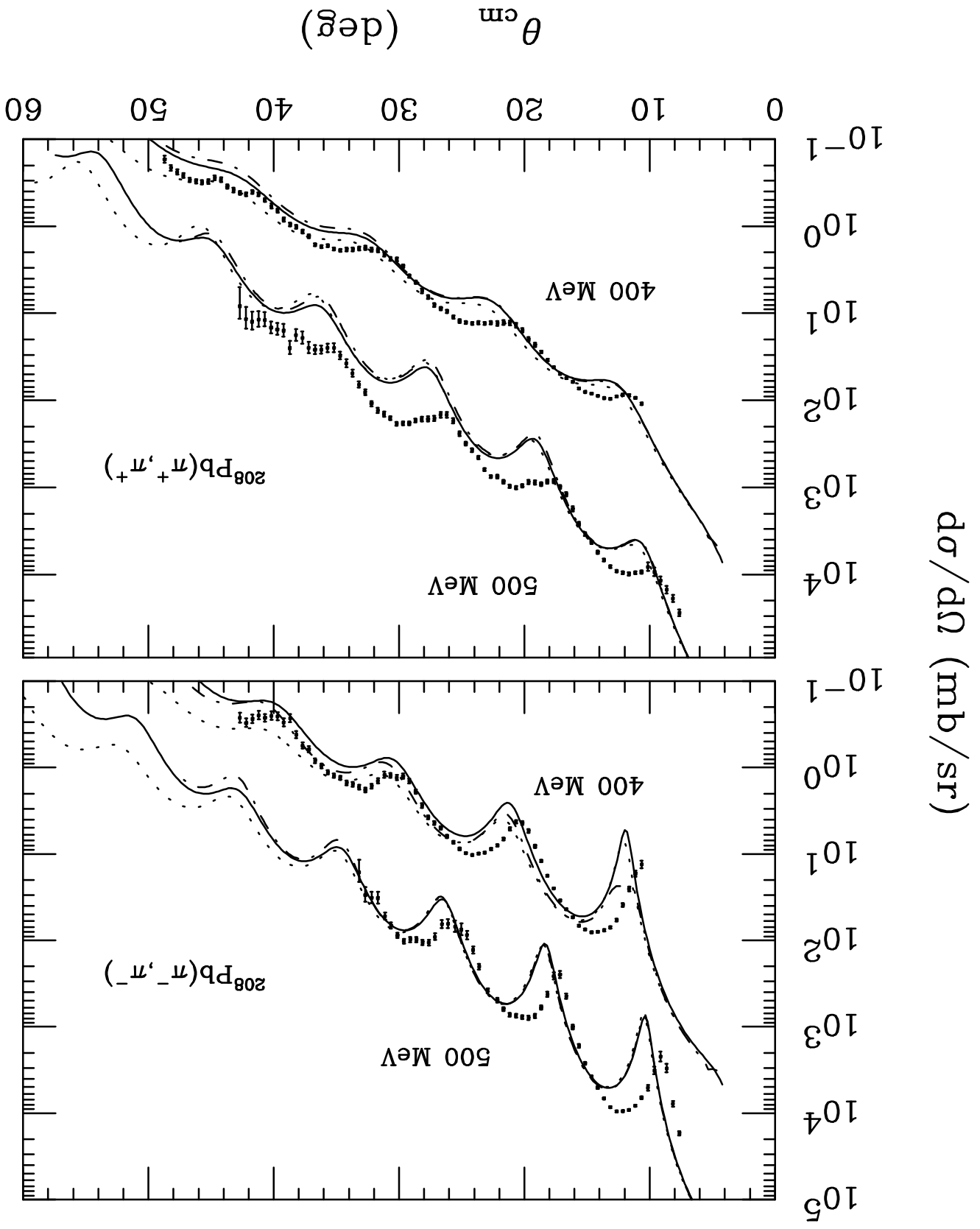
FIG. 12. $^{208}\text{Pb}(\pi^+, \pi^+)$ differential cross sections at 400, 500, and 662.7 MeV. The 400 and 500 MeV data are from this experiment and 662.7 MeV (790 MeV/c) data are from KEK. Curves are from KDP-RIA calculations.

FIG. 13. $^{208}\text{Pb}(\pi^-, \pi^-)$ differential cross sections at 400, 500, and 662.7 MeV. The 400 and 500 MeV data are from this experiment and 662.7 MeV (790 MeV/c) data are from KEK. Curves are from KDP-RIA calculations.



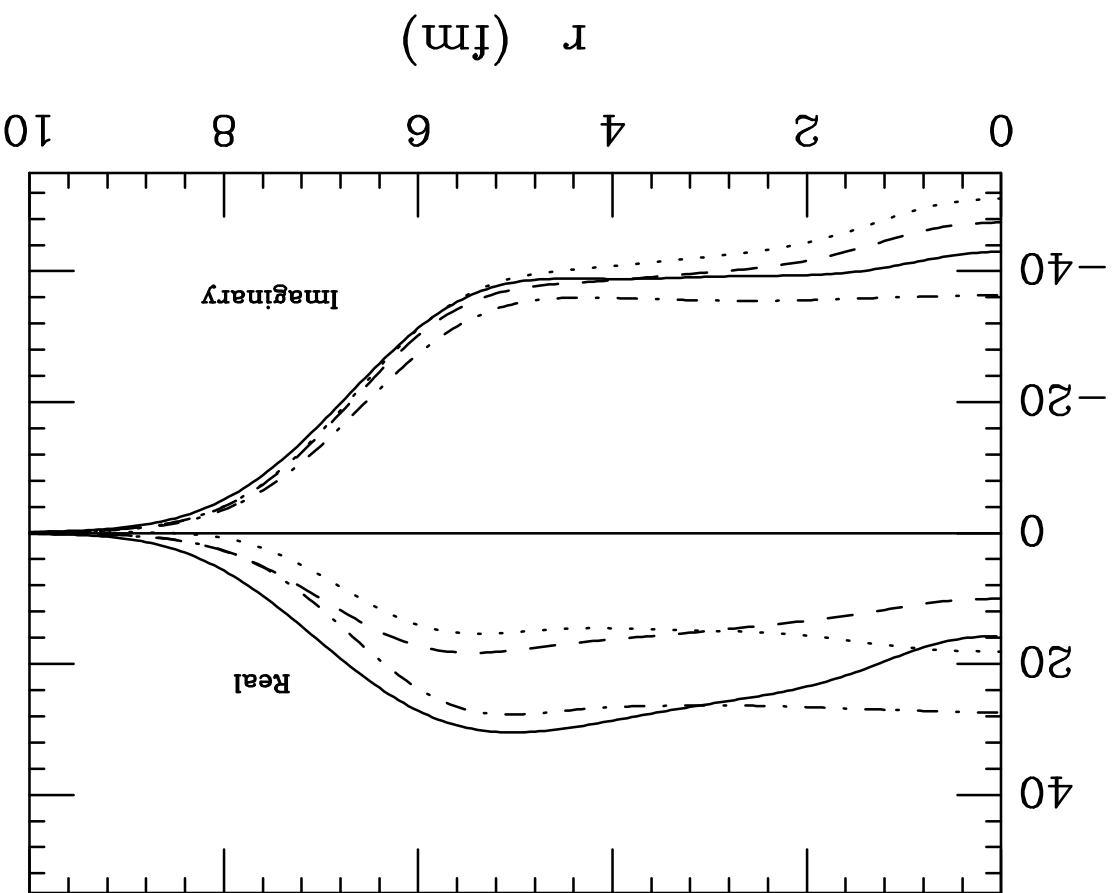






Central Potential (MeV)

$^{208}\text{Pb}(\pi^-, \pi^-)$



Central Potential (MeV)

$^{208}\text{Pb}(\pi^+, \pi^+)$

